Journal of Geophysical Research: Solid Earth

RESEARCH ARTICLE
10.1029/2018JB015581

Key Points:
- Three-dimensional coseismic displacements constrained from differential lidar topography reveal complexity in the on- and off-fault deformation
- The 36 ± 29% and 62 ± 32% of the horizontal and vertical deformation, respectively, was accommodated off the principal fault
- The off-fault deformation suggests that the elastic strain limit is exceeded over an ~250 m width in many places along the rupture

Supporting Information:
- Supporting Information S1
- Data Set S1

Correspondence to:
C. P. Scott,
cpscott1@asu.edu

Citation:
Scott, C. P., Arrowsmith, J. R., Nissen, E., Lajoie, L., Maruyama, T., & Chiba, T. (2018). The *M*7 2016 Kumamoto, Japan, earthquake: 3-D deformation along the fault and within the damage zone constrained from differential lidar topography. *Journal of Geophysical Research: Solid Earth*, *123*. https://doi.org/10.1029/2018JB015581

Received 1 FEB 2018
Accepted 27 JUN 2018
Accepted article online 4 JUL 2018

The *M*7 2016 Kumamoto, Japan, Earthquake: 3-D Deformation Along the Fault and Within the Damage Zone Constrained From Differential Lidar Topography

Chelsea P. Scott[1], J Ramon Arrowsmith, Edwin Nissen[2], Lia Lajoie[3], Tadashi Maruyama[4], and Tatsuro Chiba[5]

[1]School of Earth and Space Exploration, Arizona State University, Tempe, AZ, USA, [2]School of Earth and Ocean Sciences, University of Victoria, Victoria, BC, Canada, [3]Department of Geophysics, Colorado School of Mines, Golden, CO, USA, [4]Geological Survey of Japan, AIST, Tsukuba, Japan, [5]Asia Air Survey Co., Ltd., Kawasaki, Japan

Abstract Three-dimensional near-fault coseismic deformation fields from high-resolution differential topography provide new information on the behavior of the shallow fault zone in large surface-rupturing earthquakes. Our work focuses on the 16 April 2016 M_w 7.0 Kumamoto, Japan, earthquake, which ruptured ~40 km of the Futagawa-Hinagu Fault Zone on Kyushu Island with an oblique strike-slip mechanism and surface offset exceeding 2 m. Our differential lidar analysis constrains the structural style of strain accommodation along the primary fault trace and the surrounding damage zone. We show that 36 ± 29% and 62 ± 32% of the horizontal and vertical deformation, respectively, was accommodated off the principal fault trace. The horizontal strains of up to 0.03 suggest that the approximate elastic strain limit was exceeded over a ~250 m width in many locations along the rupture. The inelastic deformation of the fault volume produced the observed distributed deformation at the Earth's surface. We demonstrate a novel approach for calculating 3-D displacement uncertainties, indicating errors of centimeters to a few decimeters for displacements computed over 50 m horizontal windows. Errors correlate with land cover and relief, with flatter agricultural land associated with the highest displacement uncertainty. These advances provide a framework for future analyses of shallow earthquake behavior using differential topography.

1. Introduction

Observations of near-fault coseismic deformation offer insight into the processes that control the propagation of fault slip from several kilometers depth to the surface. Because the surface deformation within several kilometers of the surface rupture is commonly complex, constraints on the on- and off-fault deformation from high-resolution imagery are critical for probing the behavior of the shallow crust during earthquakes (Gold et al., 2015; Milliner et al., 2015; Nissen et al., 2012, 2014; Oskin et al., 2012; Vallage et al., 2015). Recent technical advances in imaging surface deformation from space-based and aerial platforms have led to a greater understanding of shallow on-fault slip gradients (Brooks et al., 2017; Nissen et al., 2014; Vallage et al., 2015), lithologic control on shallow fault zone architecture (Milliner, Dolan, et al., 2016; Teran et al., 2015; Zinke et al., 2014), and geometric fault zone complexities (Oskin et al., 2012). Here we image the near-fault deformation produced along the principal rupture zone of the 2016 *M*7 Kumamoto, Japan, earthquake. Our paper focuses on the performance of topographic differencing over several landscape types as well as constraints on fault zone structure inferred from fault offsets and surface strain.

The distribution of shear within fault zones and fault zone width are key parameters to understanding both the the physics that control fault propagation and the hazard imposed by active faults. Johnson et al. (1997) describe shallow fault architecture as a broad shear zone belt that is commonly hundreds of meters wide with the majority of deformation accommodated along several narrow shear zones. More recently, the term *shallow slip deficit* (e.g., Fialko et al., 2005; Simons et al., 2002) has been used to describe the inhibition of the upward propagating rupture due to off-fault inelastic yielding (Kaneko & Fialko, 2011), velocity strengthening, (Marone et al., 1991), and/or dilatancy strengthening (Segall & Rice, 1995). However, the shallow slip depletion may not be indicative of generic earthquake behavior. Xu et al. (2016) show that the shallow slip deficit may be largely an artifact of a lack of near-fault data for three earthquakes in California. Others postulate that the shallow strain missing along faults with an apparent slip deficit is accommodated as off-fault deformation with controls on the distribution of deformation from fault zone geometry, maturation, and

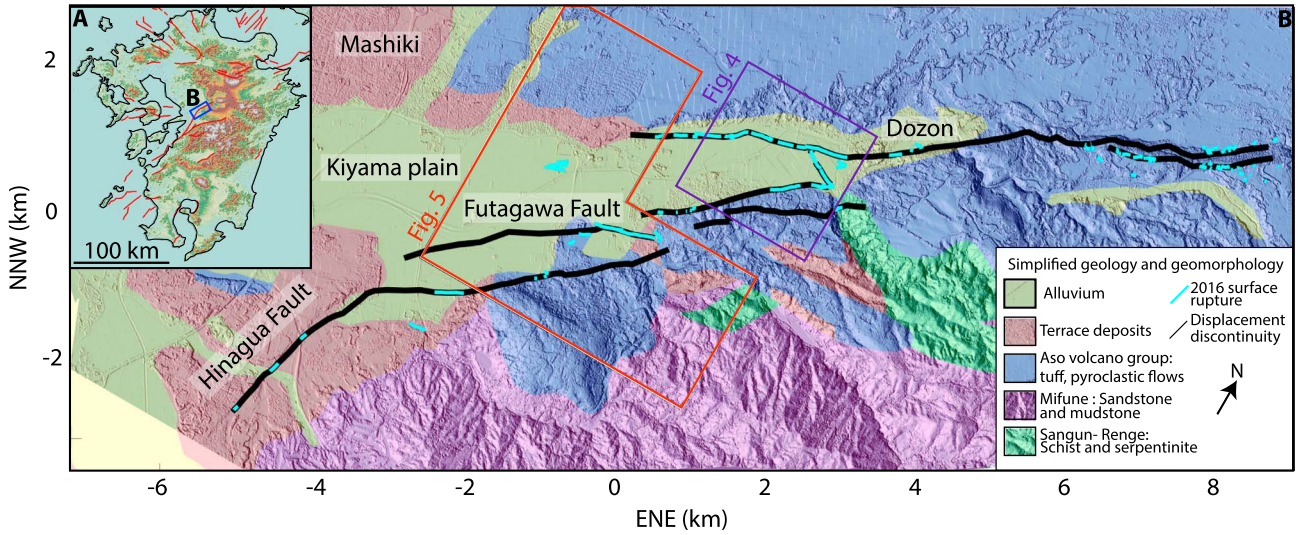

Figure 1. (a) Map of Kyushu Island with active faults in red (National Institute of Advanced Industrial Science and Technology, 2016). (b) Geologic map simplified from the Hoshizumi et al. (2004) overlain on shaded topography. Cyan lines show 2016 *M*7 Kumamoto earthquake surface ruptures visible in the postearthquake lidar imagery. Black lines show fault locations inferred from the differential lidar topography displacement discontinuity. The earthquake ruptured ~10 km beyond the northeastern limit of the lidar coverage. ENE kilometer positions are referred to in the text for convenience.

rock type (e.g., Barth et al., 2012; Dolan & Haravitch, 2014; Gold et al., 2015; Milliner, Dolan, et al., 2016; Teran et al., 2015). Observations of recent earthquakes are critical to mapping the full deformation field and ultimately understanding earthquake physics, interpreting paleoseismic and geomorphic records, and characterizing seismic hazard (e.g., Wells & Coppersmith, 1994).

The oblique strike-slip *M*7 2016 Kumamoto, Japan, earthquake produced a complex surface deformation field that is well measured with 3-D differential lidar topography, which closely brackets the earthquake and isolates the mainshock from the two largest foreshocks. Our analysis of the on- and off-fault coseismic displacement and strain fields illustrates the earthquake behavior in the upper several of kilometers of the crust. We develop an empirical technique to calculate uncertainty on the 3-D displacements, extending the work of Nissen et al. (2012, 2014). Errors range from centimeters to a few decimeters and correlate with topographic relief and land cover. To examine the on- and off-fault deformation behavior, we measure displacement discontinuities at several apertures across the fault rupture. The Kumamoto earthquake produces a maximum right-lateral and vertical surface offset of ~2 and ~1 m, respectively (Shirahama et al., 2016). Comparing the far-field (±1,000 m aperture) with the near-field (±35 m aperture) displacement discontinuities suggests that 36 ± 29% and 62 ± 32% of the right-lateral and vertical deformation, respectively, is accommodated off the principal fault. Shear strain reaches a maximum value of 0.03, and the approximate elastic strain threshold is exceeded over widths of 250 m along portions of the rupture zone. Inelastic strain begins to accumulate when the medium-field (±100 m) displacement discontinuity exceed ~0.5 m. The inelastic zone width correlates with the displacement discontinuity until the width exceeds 150 m, at which point the inelastic zone continues to widen and accommodate additional deformation without the localization of additional slip along the principal fault.

2. Tectonic Setting and the Kumamoto Earthquake

Kyushu island (Figure 1) is situated on the Eurasian plate and overlies the Nankai trough where the Philippine Sea plate subducts northwestward at a convergence rate of ~7 cm/year (Loveless & Meade, 2010). Maximum extension across the island is oriented at 147°E with a strain rate of 8.1×10^{-8} strain per year (Takayama & Yoshida, 2007). Motion along the Futagawa-Hinagu Fault Zone (FHFZ) commenced 0.7–0.5 Ma (Toda et al., 2016; Tsukuda, 1990) and is considered to be the western extension of the Median Tectonic Line (Ikeda et al., 2009; Tsutsumi & Okada, 1996); extrapolating late Holocene slip rates across the total age would imply a cumulative displacement of ~800–1,400 m (Lin et al., 2017). Volcanic activity initiated at the Aso volcano ~0.3 Ma and has produced pyroclastic and lava flows in the study area (Hoshizumi et al., 2004; Ono & Watanabe, 1985).

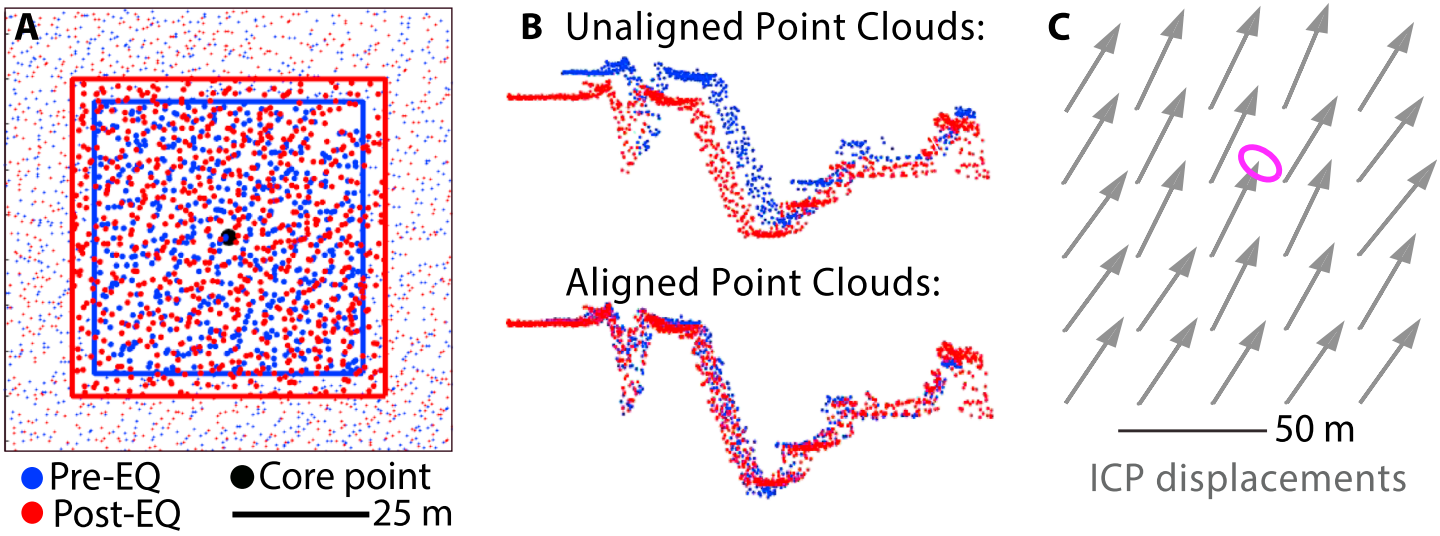

Figure 2. Outline of the 3-D displacement and rotation calculation using the Iterative Closest Point algorithm. (a) Windowed subsets of the pre-earthquake (blue) and postearthquake (red) point cloud data for the core point (black). (b) Side view showing the 3-D rigid body alignment of the two windowed data subsets (equation (1)). (c) Displacement uncertainty calculation based on the scatter in displacements at 25 core points (arrow tails) that lie over an area of 100 × 100 m^2.

The 2016 Kumamoto earthquake sequence ruptured the FHFZ on Kyushu Island of SW Japan (Figure 1). The right-lateral M_{ja} 6.5 (M_w 6.2) and M_{ja} 6.4 (M_w 6.0) foreshocks of 14 and 15 April, respectively, ruptured the northern part of the Hinagu fault (Kobayashi, 2017). The 16 April M_{ja} 7.3 (M_w 7.0) mainshock propagated ENE for ~40 km along the adjacent NNW dipping Futagawa fault, with right-lateral and normal (uplift to the southeast) motion (e.g., Lin et al., 2016; Shirahama et al., 2016). The earthquake killed over 100 people and caused intense ground shaking and damage throughout central Kyushu. Lin et al. (2017) estimate a late Holocene recurrence interval of ~1 kyr for the FHFZ with right-lateral slip rates on the Hinagu fault of 0.5–0.7 mm/year and the Futagawa fault of 1.7–2.7 mm/year with the penultimate rupture between CE 850 and 1150.

Shirahama et al. (2016) mapped surface ruptures in the 2 weeks following the 2016 *M*7 Kumamoto earthquake. They observed left-stepping en echelon cracks in rice and wheat fields of the Kiyama plain and rupture along a preexisting fault scarp tens of meters high to the east of Dozon (Figure 1). Slip is partitioned at various scales. Along part of the eastern rupture zone, Toda et al. (2016) propose that slip propagates upward along a single fault at depth and bifurcates on to the dextral Futagawa fault and the normal Idenokuchi fault (located south of the Futagawa fault, east of the lidar footprint). High geothermal gradients and low seismic velocities associated with the Aso Caldera are likely responsible for terminating the propagating rupture (Hao et al., 2017; Jiang et al., 2017; Lin et al., 2016; Uchide et al., 2016; Yagi et al., 2016).

3. Methods

3.1. Lidar Data

Asia Air Survey Co., Ldt. acquired the first lidar dataset on 15 April 2016 (Chiba, 2018a) following the foreshock activity, and the second on 23 April 2016 (Chiba, 2018b). The data were acquired with a Leica ALS5011 instrument aboard a Cessna 208 aircraft that flew at an altitude of 2,000–2,100 m above ground level. The pulse rate was 110,000 shots per second with scan angles ranging from ±22°. The footprint of the data set covers the western half of the surface rupture. The short temporal baseline between the two lidar acquisitions is ideal, because nontectonic landscape changes (e.g., vegetation growth) are minimal. To decrease artifacts from misalignment of adjacent flight paths, we remove data associated with scan angles exceeding ±18°. The resulting premainshock and postmainshock point clouds have shot densities of 2.5 and 3.5 points per square meter, respectively.

3.2. Iterative Closest Point

We use a windowed implementation of the Iterative Closest Point algorithm (ICP; Besl & McKay, 1992; Chen & Medioni, 1992) to calculate the 3-D surface deformation produced by the M_w 7.0 Kumamoto earthquake

(Figures 2 and 3). In this approach, we calculate the on-fault and off-fault displacement and rotation at a set of core points that lie on a grid with a 25 m spacing. For each core point, we select the pre-earthquake points that lie within a 50 m length square (a *window*) centered at the core point (Figure 2a). We do the same for the post-earthquake point cloud but add a 5 m buffer on each side of the post-earthquake window to ensure that the deformed pre-earthquake point cloud aligns with the post-earthquake point cloud. The optimal window dimension is a trade-off between (1) a large scale with sufficient topographic structure to produce an accurate alignment and (2) a small scale with a finer resolution that is less likely to violate the rigid body assumption (Nissen et al., 2012).

We use the LIBICP software developed by Geiger et al. (2012) to solve iteratively for the 3-D rigid body transformation that, applied to the pre-earthquake point cloud (PC_{pre}), best aligns the transformed pre-earthquake point cloud ($PC_{pre}^{transformed}$) and the postearthquake point cloud,

$$PC_{pre}^{transformed} = \begin{pmatrix} 1 & -\gamma & \beta \\ \gamma & 1 & -\alpha \\ -\beta & \alpha & 1 \end{pmatrix} PC_{pre} + \begin{pmatrix} t_x \\ t_y \\ t_z \end{pmatrix}. \quad (1)$$

α, β, and γ are rotations about the *x*, *y*, and *z* axes, and t_x, t_y, and t_z are translations in the *x*, *y*, and *z* directions. No scaling is implemented in the transformation. Equation (1) is written succinctly as

$$PC_{pre}^{transformed} = \varphi PC_{pre}. \quad (2)$$

φ is the rigid transformation,

$$\varphi = \begin{pmatrix} 1 & -\gamma & \beta & t_x \\ \gamma & 1 & -\alpha & t_y \\ -\beta & \alpha & 1 & t_z \\ 0 & 0 & 0 & 1 \end{pmatrix}. \quad (3)$$

Equations (1)–(3) are built on the assumption that the rotation (ϕ) required to align the two point clouds is small (<30°). This assumption permits the approximations $\sin(\phi) = \phi$ and $\cos(\phi) = 1$, which linearizes the transformation and allows the ICP problem to be solved with linear least squares (Low, 2004).

ICP approaches differ in their method of penalizing the solution for misalignments between the two point clouds and treatment of outliers (Rusinkiewicz & Levoy, 2001). We use the ICP point-to-plane error (*E*) to penalize for point cloud misalignment:

$$E = \sqrt{\sum_{i=1}^{\text{Pre-earthquake point cloud}} \left| \left(\varphi PC_{pre,\ i} - PC_{post,\ i} \right) \cdot n_i \right|^2} \quad (4)$$

where n_i is the vector normal to the surface at the *i*th point in the target point cloud. We prefer the ICP point-to-plane error to the ICP point-to-point error (which lacks the dot product with the normal vector in equation (4)), because of its strong penalization of vertical misfits. This is important because the topography is relatively flat compared to the horizontal extent of the ICP windows. The ICP solution converges when either the change in displacement (m) or rotation (rad) in sequential iterations is less than 10^{-4} or when 30 iterations are completed. To mitigate problems in areas of high coseismic surface disturbance, outlying points with point-to-plane misalignment errors that exceed 1 m are removed.

3.3. ICP Error

We compare two approaches for calculating ICP error over landscapes with varying topographic relief and land use. Point-to-plane error (equation (4)) is a measure of the quality of the alignment between the two point clouds. Our new error metric, displacement correlation error, is a measure of the 3-D displacement uncertainty.

3.3.1. Displacement Correlation Error

Three dominant sources of error contribute to ICP displacement uncertainty. (1) Typical 5 to 15 cm errors in the raw point cloud coordinates originate from errors in the inertial measurement unit altitude, boresight, laser

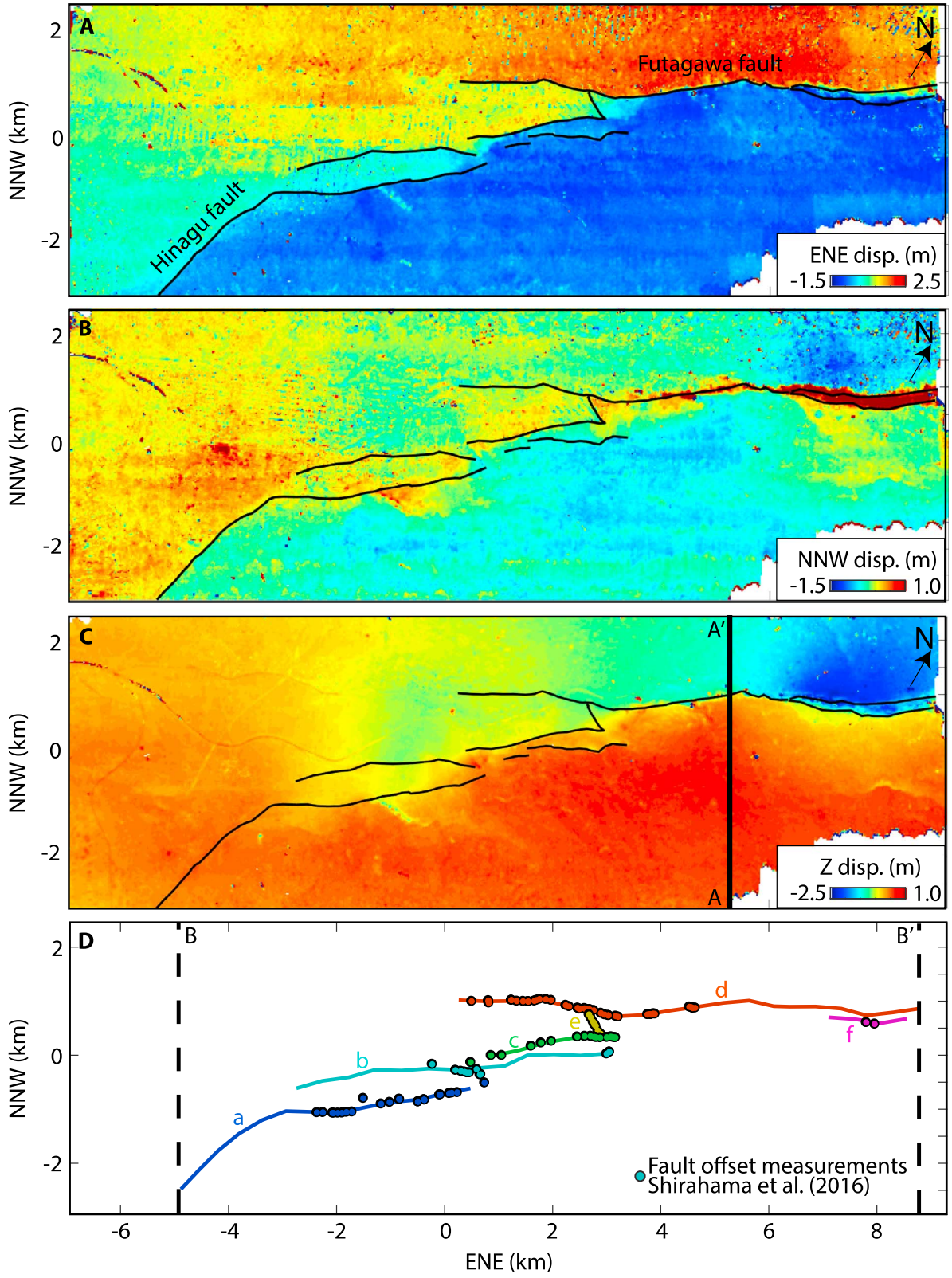

Figure 3. Iterative Closest Point displacement components for the 2016 *M*7 Kumamoto earthquake showing (a) ENE displacement, (b) NNW displacement, and (c) vertical displacement. Black lines show faults mapped as the displacement discontinuity. Note the effect of the flight path (nearly parallel to the long axis of the figures) overlap in the horizontal displacement field. Surface displacement along the A-A′ profile is shown in Figures 6c and 6d. (d) Is a simplified rupture map labeling fault segments shown in Figure 7. Dashed lines indicate the boundaries of the B-B′ transect in Figure 8.

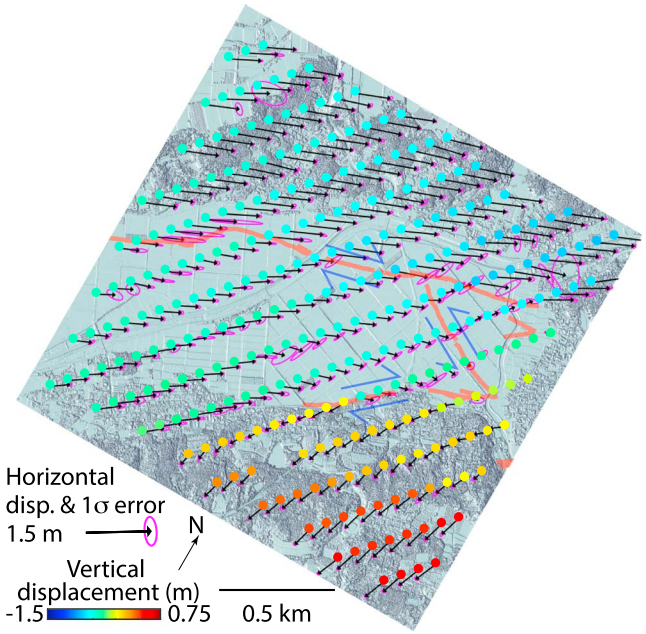

Figure 4. Coseismic surface displacements along a conjugate shear zone with 1σ errors on the horizontal surface displacements shown by pink ellipses. Figure location shown in Figure 1. Orange lines show faults activated in the 2016 earthquake mapped from the post-earthquake lidar imagery.

scanner, lever arm offset, and dGPS kinematic position (Glennie, 2007; Toth et al., 2007). These errors are observed along the flight path overlap (e.g., the ENE oriented linear patterns in Figure 3). (2) The sensitivity of the surface displacement measurement using ICP depends on the local topographic relief. For example, point cloud windows over flat or planar topography can be well aligned with a range of rigid deformations, rendering the inferred displacements spurious as suggested by Nissen et al. (2012). (3) Changes in landscape shape from coseismic damage and vegetation growth make the precise alignment of the two datasets impossible. Our removal of individual points with ICP point-to-plane error (equation (4)) exceeding 1 m partially mitigates this latter problem. Further, changes in vegetation are minimal due to the 8 day time span between the lidar acquisitions. Because the dense forests in parts of the study area result in very few ground returns, we perform ICP calculations on unfiltered point clouds instead of on ground classified points, counter to the suggestion of Ekhtari and Glennie (2017).

We develop the displacement correlation error calculation to quantify the effect of error sources (2) and (3) described above on the displacement uncertainty. To calculate the error at a given core point, we consider the 24 surrounding core points that lie on the same side of the fault within a 100×100 m^2 area (Figure 2c). To limit true surface strain leaking into the estimated scatter, we remove planar ramps from the displacements in each Cartesian coordinate direction. We calculate the 1σ error ellipse from a principal component analysis of the horizontal displacements. The 1σ vertical errors are the standard deviation of the vertical displacements. Results along the conjugate shear zone near Dozon (Figure 1) described by Lin and Chiba (2017) and Shirahama et al. (2016) are shown with horizontal error ellipses in Figure 4. Although a full treatment of the three sources of error described above is beyond the scope of this paper, our analysis described below demonstrates that the ICP displacement correlation error quantifies the quality of ICP displacements over different landscape types.

3.3.2. ICP Errors and Land Use

We explore the relationship between topographic relief, land use, and the two types of ICP errors over a subset of our study area. Figure 5a shows the standard deviation of the point cloud elevations over square windows with 50 m lengths over agricultural landscapes, built-up areas of Mashiki town, and high-relief forests. Figure S2 shows the errors in map-view. The ICP point-to-plane error (equation (4); Figure 5b) scales with topographic roughness. The 5 to 10 cm errors in the agricultural lands reflect the ease of aligning relatively flat topography. The 20 to 45 cm errors over built-up areas of Mashiki are partially due to coseismic infrastructure damage (Figure S2; Goda et al., 2016; Moya et al., 2017), which make a precise alignment of the two point clouds impossible. The 20 to 35 cm errors in the mountains reflect the challenge of point cloud alignment over rough landscapes and the effect of different illuminations of geometrically complex objects such as trees. In contrast, the horizontal ICP correlation error (3.3.1 above) scales inversely with topographic relief (Figure 5c), suggesting an anticorrelation between the two error types. The median 1σ horizontal correlation error of 6–10 cm in agricultural landscapes reflect the range of rigid transformations that produce satisfactory alignments of fairly featureless topography. The high degree of relief over the mountains results in a more accurate alignment of the two point clouds. The median vertical ICP correlation error (Figure 5d) ranges from 1 to 3 cm with minor correlation to land use. The vertical error is lower than the horizontal error, because (1) the alignment of the window centroids commonly produces a quality vertical displacement and (2) point cloud errors are lower in the vertical dimension (Glennie, 2007; Toth et al., 2007). For assessing the relative quality of ICP displacements, we prefer the ICP correlation error over the ICP point-to-plane error because the former is indicative of the relative displacement accuracy.

4. Displacement Discontinuity

To examine along-strike variations in on- and off-fault deformation, we use a displacement discontinuity calculation to estimate surface offset over near- (±35 m), medium- (±100 m), and far-field (±1,000 m) fault

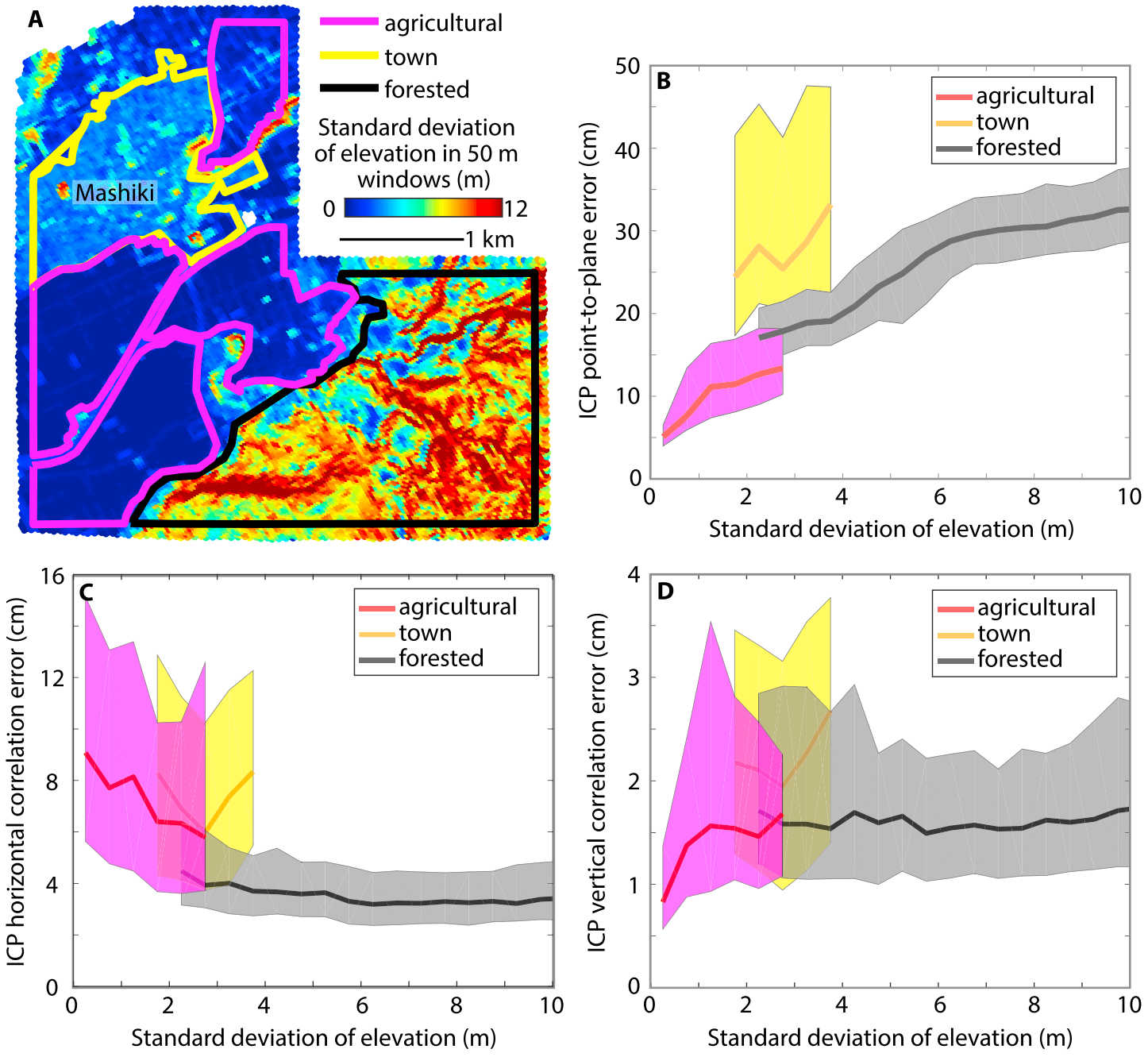

Figure 5. The correlation between Iterative Closest Point (ICP) error and topographic relief. (a) Standard deviation of elevation over 50 m windows calculated from the lidar point clouds as a measure of topographic roughness. Colored lines show agricultural (pink), urban (yellow), and forested (black) landscapes. (b) ICP point-to-plane error (equation (4)) versus the standard deviation of elevation for the three landscape types. Lines show the median 1σ error, and clouds show the 16th to 84th error percentiles (i.e., 1σ) in the given standard deviation of elevation bin. (c) Mean horizontal (i.e., average of major and minor ellipse axes lengths). (d) vertical displacement correlation error.

normal apertures as shown in Figure 6. The near-field calculation is performed as follows (Figure 6a): At 25 m increments along the fault trace, we align the ICP coordinate system with the local fault strike. We calculate 3-D displacements at two core points $\mathbf{d_{1,35}}$ and $\mathbf{d_{2,35}}$ each located 35 m from the fault trace on opposite sides of the fault. The right-lateral displacement discontinuity at the 35 m aperture ($d_{r,\ 35}$) is the differential displacement projected onto a horizontal unit vector parallel to the fault strike,

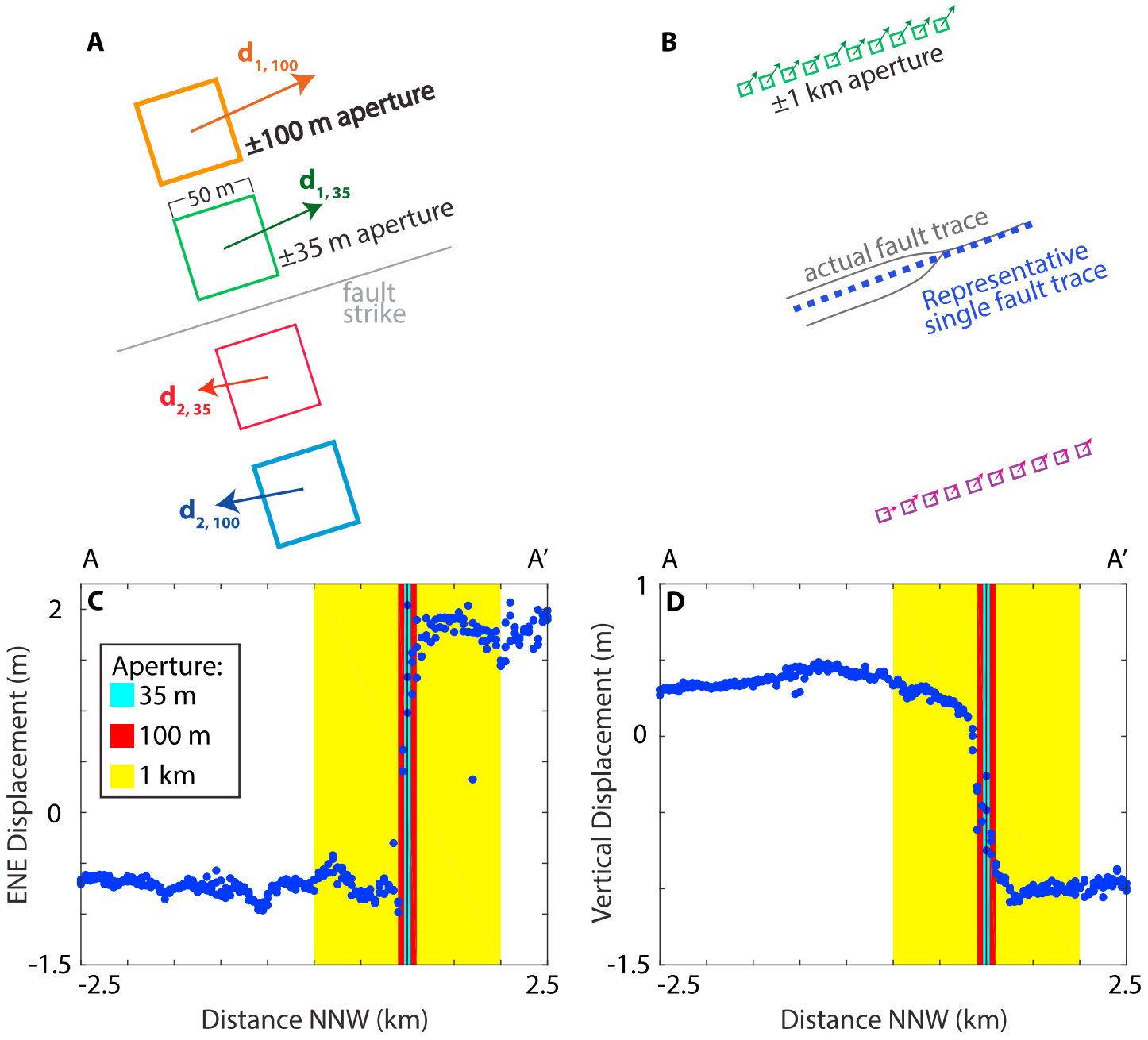

Figure 6. Displacement discontinuity calculation. (a) Map view illustration of the displacement discontinuity calculation over ±35 m (green and red boxes) and ±100 m (orange and blue boxes) apertures. (b) Displacement discontinuity over the ±1 km aperture where the boxes are placed 1 km on either side of a fault or from the center of a bifurcated fault. (c) ENE and (d) vertical displacement profiles highlighting the apertures used in the displacement discontinuity calculation along the A-A′ profile location in Figure 3c.

$$d_{r,35} = \left(\mathbf{d_{1,35}} - \mathbf{d_{2,35}}\right) \cdot < \text{fault strike} > . \tag{5}$$

The vertical displacement discontinuity at the 35 m aperture ($d_{v,35}$) is the differential displacement projected onto a vertical unit vector,

$$d_{v,35} = \left(\mathbf{d_{1,35}} - \mathbf{d_{2,35}}\right) \cdot < 0, 0, 1 > . \tag{6}$$

The ±100 m aperture calculations are identical except that the core points are spaced 100 m from the fault trace. To calculate the displacement discontinuity at an aperture of 1 km, we construct a line that bisects

the fault traces (Figure 6b), align the ICP coordinate system with this line, and calculate displacements at core points located 1 km from the bisecting line.

Figures 6c and 6d show the spatial extent of the displacement discontinuity calculations on displacement profiles. Most right-lateral deformation is localized along the fault plane and captured by the near- and medium- field measurements. The vertical profile shows subsidence of the northwestern block constrained by the near- and medium- field measurements and off-fault warping captured by the far-field measurement.

Fault offsets are commonly calculated by fitting a line to displacement profiles on either side of the fault and extrapolating this line to the fault (e.g., Milliner et al., 2015; Rockwell et al., 2002; Treiman et al., 2002). We compare our discontinuity approach to this approach in Figure S3 for several cases of forward slip models (Okada, 1985) with gradients in on-fault slip and secondary faulting. Both approaches can distinguish between cases of uniform slip localized to a fault plane and distributed deformation. For the Kumamoto earthquake, we prefer the displacement discontinuity calculation, because the approach avoids line fitting across warped regions (e.g., Figure 6d) and constrains deformation at explicit spatial scales.

We calculate off-fault deformation (OFD) as the difference in the near- and far-field displacement discontinuities normalized by the far-field displacement discontinuity:

$$\mathrm{OFD} = (\mathbf{d_{1000}} - \mathbf{d_{35}})/\mathbf{d_{1000}}. \quad (7)$$

The histograms in Figure S6 show the percentage of total deformation accommodated as OFD with uncertainty reflecting the standard deviation in OFD. We are effectively equating the near-field displacement discontinuity with on-fault deformation. While this assumption may underestimate the inferred OFD relative to a comparison with field data, the spatial continuity of the displacement discontinuity estimate allows this calculation to be representative of the entire fault and to be unbiased by different measurement techniques.

5. Coseismic Strain

We examine the magnitude and orientation of the 2-D (horizontal) strain field to constrain the distribution of deformation and possible rheological controls on its surface expression. We calculate the horizontal strain tensor using a similar approach to Allmendinger et al. (2009, 2012). We solve for the 2-D displacement gradient tensor ($\boldsymbol{e}_{ij}$) from horizontal displacements at 25 core points over an area of 100 × 100 m^2 centered around the core point of focus. We apply an inverse weighting based on the ICP displacement correlation error and solve for the 2-D strain tensor using a weighted least squares inversion (Menke, 1984). We solve for ε_{ij} (i.e., the symmetric component of $\boldsymbol{e}_{ij}$) and plot its first tensor invariant ($\varepsilon_{\mathrm{min}} + \varepsilon_{\mathrm{max}}$) in Figure 9a. Figure 9b shows the shear strain (e_{12}). Note that shear strain is not basis invariant: we calculate the shear strain along the 060–330 oriented coordinate system that is approximately aligned with the Futagawa fault and along which the peak surface displacements in the Kumamoto earthquake occurred. We use 0.5% as the elastic limit of rocks (e.g., Brooks et al., 2017), which is the approximate ratio of the yield stress to Young's modulus for a variety of hard rocks. To solve for the principal strain orientation, we perform an eigenvector decomposition of the strain tensor. We decrease noise in the orientations by calculating the mean Fisher orientation (Fisher et al., 1987) over a moving 100 × 100 m^2 window. We plot only the orientations at core points within 100 m of the fault traces and with strain exceeding 0.1% (Figure 10). We calculate the angle (θ) between the principal extension direction and the fault orientation with spread that reflects the 95% Fisher uncertainty cone. Additional details on the strain calculation are given in the supporting information.

6. Results

6.1. Fault Geometry and Displacement Discontinuity

The 3-D ICP displacement field shows that the Kumamoto earthquake accommodated right-lateral and northwest side down motion (Figure 3), in agreement with earlier results (Moya et al., 2017; Shirahama et al., 2016; Toda et al., 2016). The ICP analysis also reveals sections of off-fault deformation that were not mapped in the field. Here we describe the geometry and deformation associated with the shallow rupture starting from its southwest end and moving northeastward in the direction of rupture propagation. Throughout the description the reader is referred to the local geology in Figure 1, the deformation field in Figure 3, and the offset profile in Figure 7; and all localities are given as distances along the *x* axes of these figures.

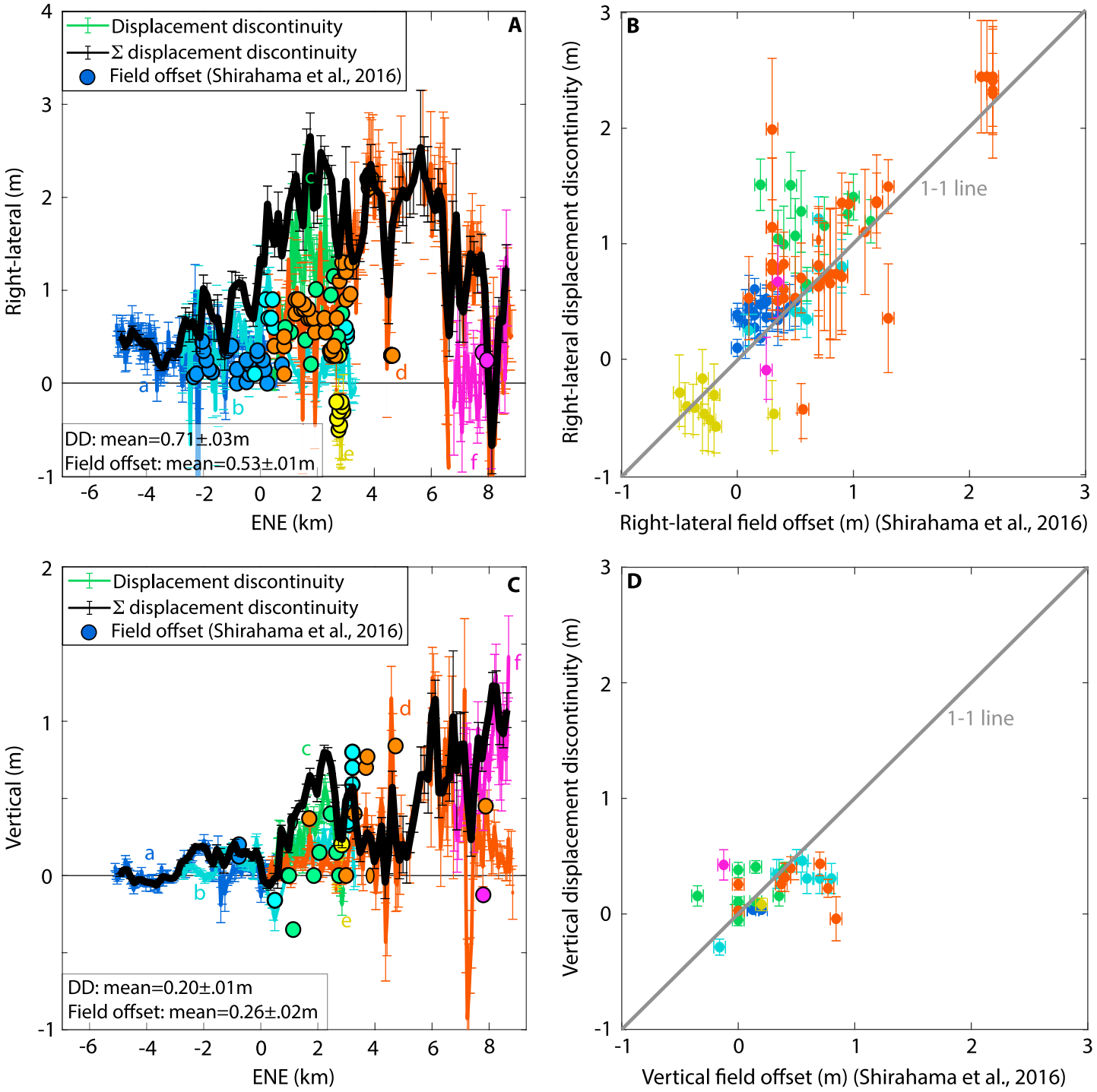

Figure 7. Displacement discontinuity and field offset measurements. (a) and (c) Colored curves: Displacement discontinuity at an aperture of ±35 m with 1σ error. Thick black lines show the summed slip across faults within a 250 m moving average window. Dots are field measurements from Shirahama et al. (2016). The mean displacement and offset measurements reflect only observations where the data types are colocated. Positive vertical indicates southeast side-up motion. Colors correspond to the fault traces shown in Figure 3d. (b) and (d) Comparison of displacement discontinuity and field fault offset measurements from Shirahama et al. (2016) with a one-to-one gray line.

The northeast striking Hinagu fault, located in the southern extent of Kiyama plain, accommodated ~0.5 m of right-lateral displacement discontinuity and negligible vertical deformation (Figures 3 and 7). The rupture steps to the right onto two subparallel segments of the Futagawa fault (Figure 3: eastern end of segment a, segment b) that together accommodate ~1 m of right lateral and ~0.5 m of vertical displacement discontinuity. At kilometer 1, at the eastern end of Kiyama alluvial plain (Figure 1), the earthquake activates two fault segments that join in a conjugate shear zone (segments c–e) as reported by Lin and Chiba (2017) and Shirahama et al. (2016). Slip continues for 2 km along segment d where the fault accommodates a maximum 2.3 m displacement discontinuity (Figure 7). Within the pyroclastic flow unit at 7 km (Figure 1), the fault rupture bifurcates into northern and southern ruptures that accommodate dominantly right-lateral and vertical motion, respectively. The summed displacement discontinuity curve (black line in Figure 7) varies smoothly, suggesting that complexities in the surface fault geometry and slip variability mask a simpler pattern of energy release at depth.

We compare field measurements of fault offset (Shirahama et al., 2016) to the near-field (±35 m) lidar displacement discontinuity to examine variations in shallow fault behavior (Figures 7b and 7d). While both datasets show similar deformation trends, the average right-lateral lidar displacement discontinuity exceeds the surface offset by 33% with nonoverlapping uncertainties. The best agreement between the two measurement types occurs along segments a, b, e, and f (Figure 7). Larger differences occur along segments c and d within the agricultural lands of the Kiyama plain where the tensional cracks and mole tracks observed in the field (Shirahama et al., 2016) suggest complexity in the near-fault deformation.

The near-, medium- and far-field displacement discontinuities are indicative of slip at increasing depths as well as off-fault deformation at greater distances from the fault, as shown in Figures 8a–8c. The first-order horizontal and vertical deformation patterns show increasing deformation with greater aperture. Within the zone of fault bifurcation (NE end of Figure 3), the deformation is distributed within the medium and far-field apertures. Overall, the right-lateral and vertical far-field displacement discontinuities exceed the near-field displacement discontinuity by 36 ± 29% and 62 ± 32%, respectively. We explore a potential lithologic control on the correspondence between the near- and intermediate-field displacement discontinuities (Figures 8d, 8e, S4, and S5). For larger amounts of deformation, we observe an increase in the intermediate-field relative to the near-field displacement discontinuity for the three types of lithologic fault contacts. The largest difference in the displacement discontinuity at the two apertures occurs in the fault bifurcation zone along the volcanic-to-volcanic fault contact.

6.2. Horizontal Strain Field

Figure 9a shows the first invariant of the 2-D strain tensor (i.e., area change). The black lines contour the region where the elastic strength of hard rocks is exceeded (section 5). The inelastic deformation is apparently negligible west of kilometer 0, where right-lateral displacements along individual faults are $<$0.5 m. In the zone of fault bifurcation (NE end of Figure 9a), the inelastic zone is up to ~500 m wide, with extension concentrated along the southern normal fault and contraction along the northern right-lateral fault. The shear strain (Figure 9b) is nonnegligible along the full length of the rupture, reaching 3% from kilometers 3 to 6 (coincident with peak slip of 2 m on segment d). The maximum shear strain decreases in the zone of fault bifurcation where deformation becomes more distributed. The first strain invariant extends over a broader aperture than the shear strain (Figure 9c). This suggests that processes associated with off-fault dilation and contraction act over apertures that extend beyond areas of concentrated shear. Although we do not explicitly calculate vertical strains, the distributed vertical deformation also suggests that off-fault deformation processes are associated with vertical deformation.

The relationship between the displacement discontinuity and the width of the inelastic zone is quantified with two best-fit lines to the data west of the fault bifurcation (Figure 9d; green dots). Approximately 50 cm of displacement discontinuity is required to accumulate significant inelastic deformation. The inelastic zone widens with increasing displacement discontinuity until the zone reaches ~150 m in width. The width of the inelastic zone continues to increase with additional deformation accommodated as distributed strain that is not localized to the primary fault.

We examine the relationship between the principal strain orientations and regional deformation trends (Figure 10). Along the Hinagu fault, the maximum extension axis is oriented NNW, aligned with the

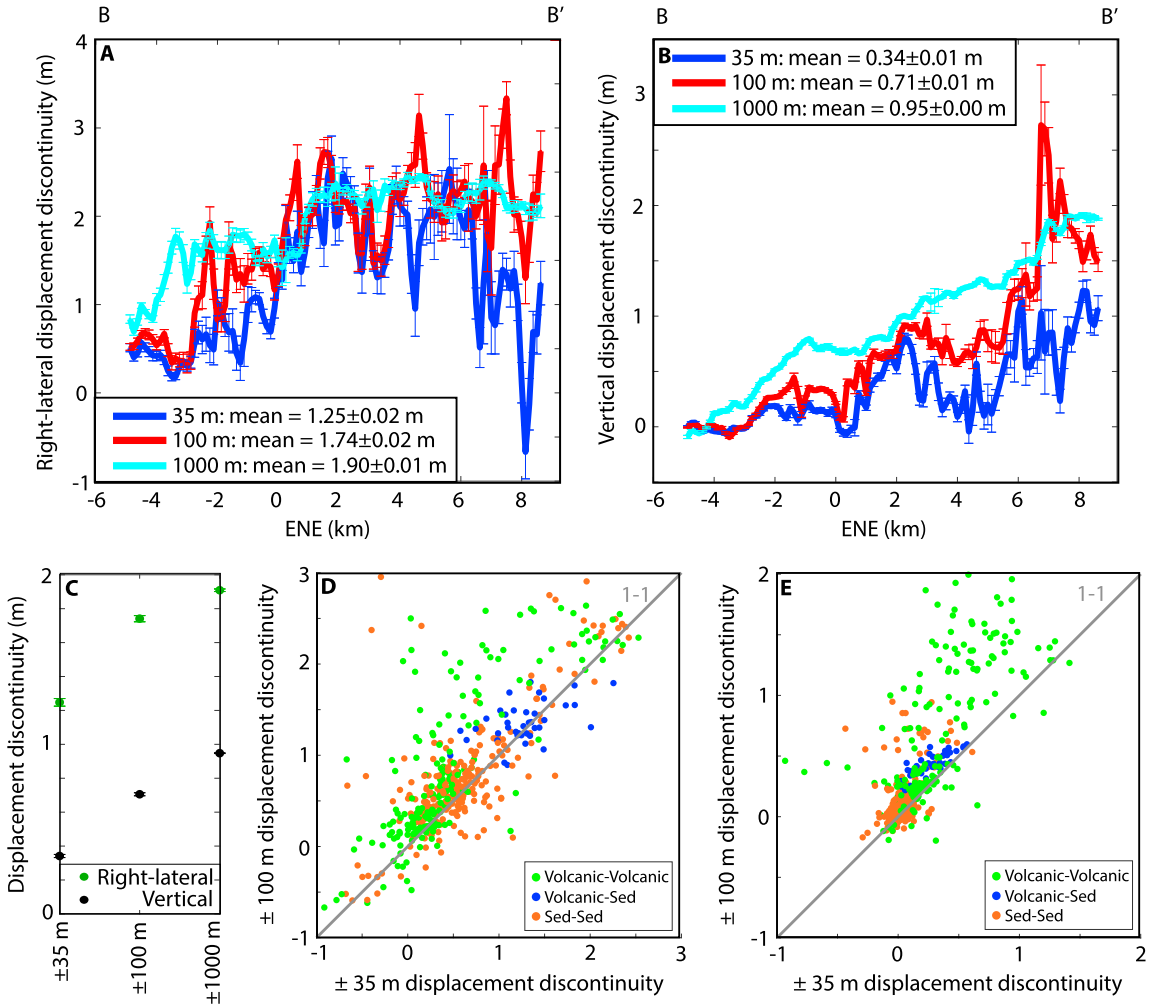

Figure 8. Right-lateral (a) and vertical (b) displacement discontinuity along the main rupture zone at apertures of ±35 m (dark blue), ±100 m (red), and ± 1,000 m (cyan). The location of the along-strike B-B′ transect is shown in Figure 3d, and Figure 6 illustrates the displacement discontinuity calculation at different apertures. (c) Average right-lateral (green) and vertical (black) displacement discontinuity at the ±35, ±100, and ±1,000 m apertures. The ±100 m versus ±35 m (d) right-lateral and (e) vertical displacement discontinuities along volcanic-volcanic (green), volcanic-sedimentary (blue), and sedimentary-sedimentary fault contacts (orange). The gray line is the one-to-one line.

regional extension axis of 327° (Takayama & Yoshida, 2007). When the rupture steps to the Futagawa fault, the maximum extension axis rotates to a N-S orientation, oblique to the regional extension direction. When the fault bifurcates, the northern and southern faults (segment d and segment f in Figure 3) accommodate NNW and NE extension, respectively. Strain orientations thus vary over the kilometer scale in the individual earthquake and may be oblique to the regional strain directions. The variation in deformation behavior likely reflects local structural complexity and mechanical interactions with neighboring faults (e.g., Pollard et al., 1993; Riller et al., 2017) and possibly also with volcanic sources associated with Mt. Aso Volcano located to the east.

7. Discussion

7.1. Calculating Near-Fault Displacements From ICP

Differential high-resolution topography and the ICP algorithm can be used to reliably resolve near-fault 3-D deformation, building on the work of Nissen et al. (2012, 2014). We estimate similar errors to the synthetic tests on real *B4* (San Andreas fault) point clouds by Nissen et al. (2012) and lower errors than Nissen et al. (2014) determined on lidar digital terrain models spanning the 2011 Fukushima-Hamadori, Japan,

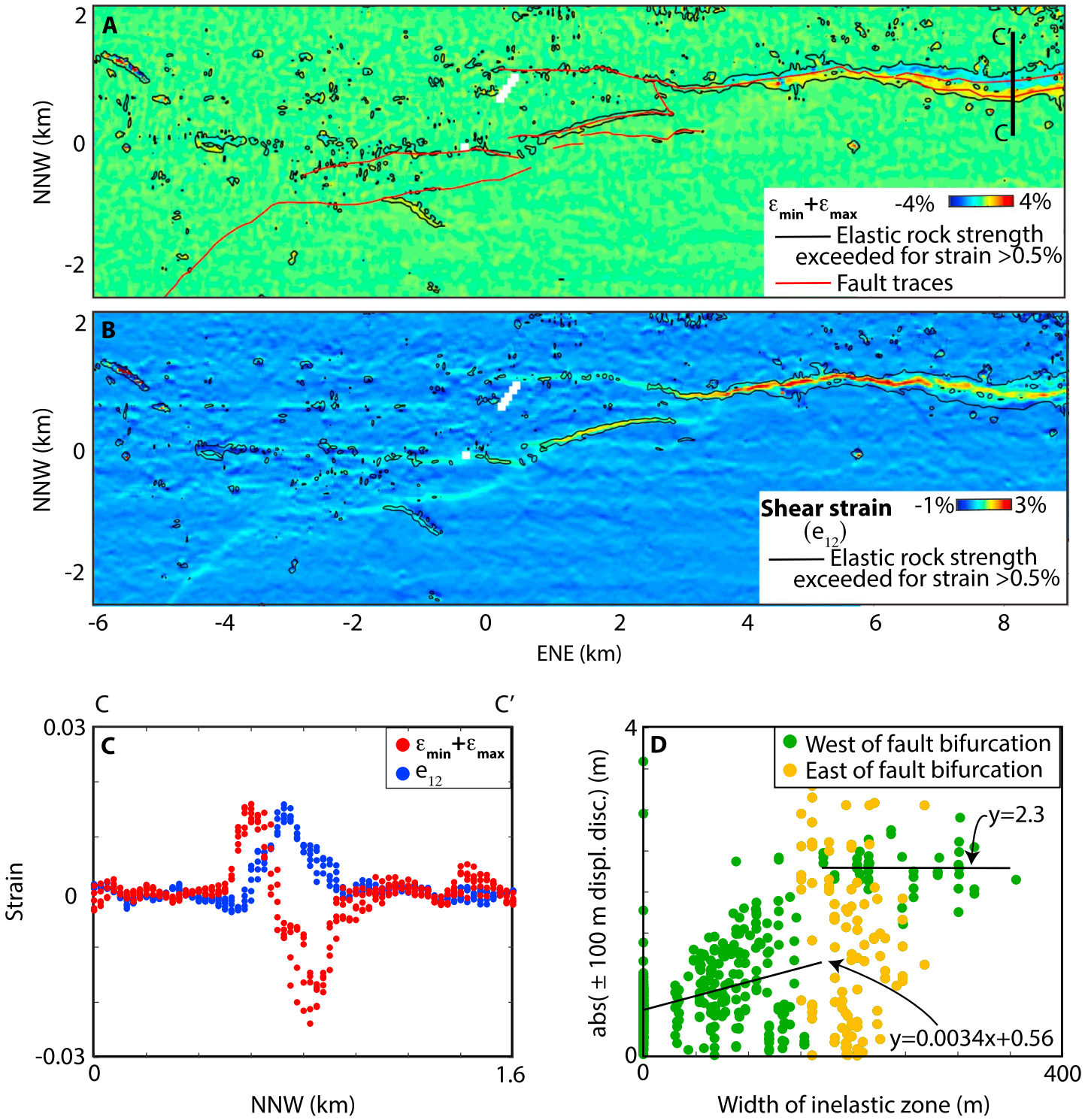

Figure 9. Horizontal strain: (a) First invariant of the 2-D strain tensor ($\varepsilon_{min} + \varepsilon_{max}$). Positive strain denotes extension, and negative strain denotes contraction. The black line contours areas where either principal strain component exceeds 0.5%, the approximate elastic strain limit for a range of hard rocks. (b) Shows the 2-D shear strain (e_{12}) in the figure coordinate system and the 0.5% black contour of the first invariant of the strain tensor (identical to (a)). Positive indicates right-lateral strain. (c) Shows the first invariant of the strain tensor (red) and the shear strain (blue) along the C-C′ transects in Figure 9a. (d) The 100 m displacement discontinuity versus the width of the inelastic zone. Green dots reflect locations west of the fault bifurcation (at kilometer 6.5). The two lines are fit to the green points only. Orange dots show points within the fault bifurcation zone. Displacements represent activity on one of the two faults, and the width is half of the total width of the inelastic zone.

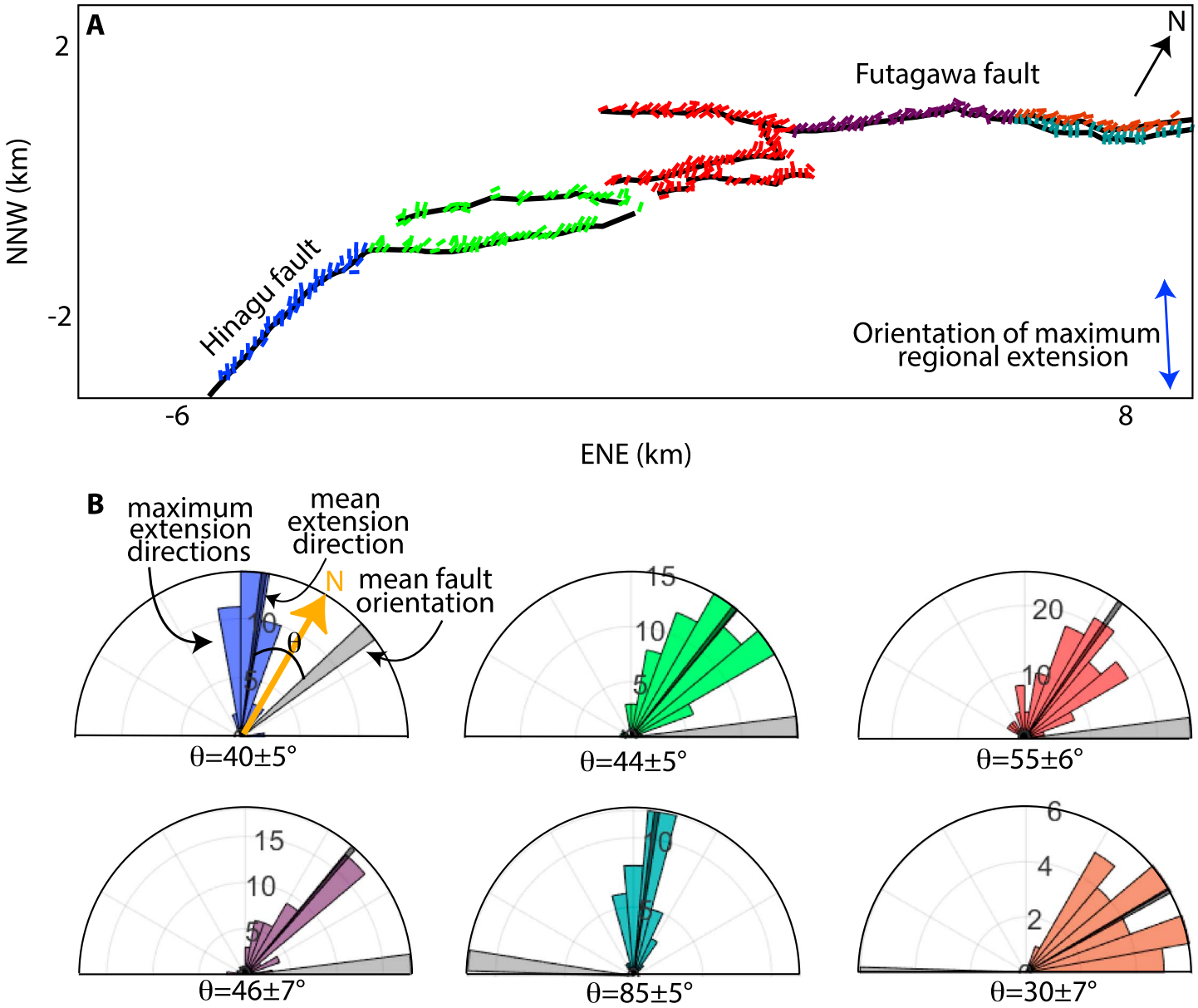

Figure 10. Orientation of maximum 2-D extension. (a) Tick marks show the orientation of the maximum horizontal extension, and colors denote different fault traces. Note the orientation of the north arrow. The blue arrow shows the GPS-calculated orientation of regional maximum extension (Takayama & Yoshida, 2007). (b) Rose diagrams showing the distribution of the maximum extension directions (colored petals), mean maximum extension direction (thin black petal), and the mean fault orientation (thick gray petal) for each fault segment. The orientation of the north arrow is the same as in panel a. θ is the angle between the principal extension direction and the fault orientation, and the quoted uncertainty is 2σ.

earthquake. The similar errors between this Kumamoto study and Nissen et al.'s (2012) analysis likely reflect the similar point density and the minimal effect from vegetation. The higher error of Nissen et al. (2014) likely reflects their lower spatial resolution, particularly of the pre-earthquake data set, as well as the multiyear time span between acquisitions. It remains unclear whether performing ICP calculations on unfiltered or filtered (e.g., ground returns only) point clouds results in the highest quality displacements. Likely, the answer is a balance of the temporal baseline between the two acquisitions (and thus the amount of vegetation change) and the vegetation density (results based on ground return points are meaningless in a dense tree canopy with few ground returns). Our error estimation approach provides a means for assessing which approach is best.

7.2. Displacement Discontinuity Along the Primary Fault Trace

For the 2016 *M*7 Kumamoto earthquake, the differential displacement increases with aperture from 35 to 1,000 m. Because the elastic strain threshold is exceeded by a factor of 5–10, we propose that the larger displacement discontinuity with aperture relationship reflects off-fault and inelastic deformation that may be coupled with a shallow depletion of on-fault slip. Likely, the off-fault deformation is accommodated along secondary fractures and folds. The relationship between slip and inelastic zone width is nonlinear (Figure 9d): The initial deformation is accommodated as slip localized to the fault plane. Intermediate amounts of deformation accrue slip as on the fault primary fault plane as well as distributed off-fault strain. Once a deformation threshold is exceeded, off-fault deformation dominates.

Brooks et al. (2017) show that the coseismic slip along the principal fault trace for the 2014 M_w 6.0 Napa earthquake terminates 3 to 25 m below the surface, possibly reflecting ductile deformation of unconsolidated surface materials. In contrast to our results, they argue that the depleted slip is not accommodated along secondary structures. The difference in behavior between the Napa and Kumamoto earthquakes may reflect earthquake magnitude. It is not too surprising that the lower magnitude Napa earthquake did not rupture the surface. The larger magnitude Kumamoto earthquake ruptured the surface and caused the wider fault zone to accumulate plastic deformation once the elastic strength of the fault rock was exceeded. Similar to our results, Nissen et al. (2014) observe a shallow depletion of slip for the surface rupturing 2011 M_w 6.6 Fukushima-Hamadori, Japan, earthquake (up to 2 m slip in the investigated portion) and also suggest that the missing slip is likely redistributed onto folds and secondary faults.

7.3. Off-Fault Deformation

Dolan and Haravitch (2014) suggest that structurally immature faults ($<$25 km of total offset) and mature faults ($>$85 km) localize ~50–60% and 85–90%, respectively, of the total deformation along the fault trace. Our estimate that 64 ± 29% of the total horizontal deformation of the Kumamoto earthquake was accommodated on the principal fault is consistent with these predictions, although our approaches for calculating off-fault deformation differ. Interestingly, the vertical deformation for the Kumamoto earthquake is approximately half as localized (twice as distributed) as the horizontal deformation; this observation is shown in both the quantitative estimates of on-fault deformation and qualitatively in the 3-D displacement fields (Figure 3). On the assumption that the far-field deformation reflects elastic deformation due to fault slip at depth, we infer that the variation in the distribution of horizontal and vertical deformation signifies a vertical gradient in rake along the primary fault plane from oblique slip at depth to dominantly right-lateral slip within the very shallow subsurface. This suggestion may reflect an anistropy in the material properties that cause the rocks to fail faster when subjected to the stresses that drive vertical deformation.

The largest differences between the near- and medium-field displacement discontinuity occur within the zone of fault bifurcation near the town of Dozon where the fault ruptures through tuff and pyroclastic flows (Figures 1 and 8). The complex fault geometry created by the overlapping fault segments may explain the distributed nature of the deformation, as other authors (e.g., Milliner, Dolan, et al., 2016; Milliner, Sammis, et al., 2016) have correlated geometric fault complexity with distributed deformation. Shallow rock type is commonly cited as a secondary control on the distribution of deformation. Softer rocks are commonly associated with enhanced distributed deformation (Milliner, Dolan, et al., 2016; Teran et al., 2015; Zinke et al., 2014). For the Kumamoto earthquake, we consider that the volcanic rocks near Dozon may indeed be quite weak, particularly if they are heavily fractured or weathered. However, drill logs suggest that pyroclastic flows and lavas underlie the alluvium within the Kiyama plain at a few tens of meters depth (Watanabe et al., 1979). The extrusive volcanic rocks may exert a dominant control on the shallow surface deformation even where the surface cover is alluvium.

7.4. Fault Zone Structure

The Kumamoto earthquake produced distributed off-fault and inelastic deformation over widths of ~250 m with strain maximized along narrow fault zones. The near-fault regions that deformed inelastically in the 2016 earthquake likely spatially overlap with the compliant fault damage zone created by many past ~*M*7 earthquakes on the FHFZ. Future imagery differencing at still-higher spatial resolution may facilitate examining whether the fault zone is best described as a block model with decreasing block dimension and material

rigidity toward the principal fault (e.g., Shelef & Oskin, 2010) or as a broad shear belt with areas of localized deformation (e.g., Johnson et al., 1997).

Off-fault cracking is likely an important mechanism in the accommodation of extension within the zones of inelastic deformation (Figure 9). Seismic observations have demonstrated a seismic velocity reduction within the upper few hundred meters of fault zones, which is often attributed to the opening of cracks (e.g., Ben-Zion et al., 2003; Li et al., 2006; Li & Leary, 1990). Further, the physical properties of the damage zone vary significantly along strike (Lewis & Ben-Zion, 2010). Ultimately, it is critical to couple observations of surface deformation with computational models that include complex crustal rheology to understand controls on variations in the surface deformation field and their relationship to fault zone structure (e.g., Brooks et al., 2017; Roten et al., 2017).

8. Conclusion

We calculate 3-D coseismic displacements for the *M*7 2016 Kumamoto, Japan, earthquake from pre-earthquake and post-earthquake high-resolution differential lidar topography. These data reveal valuable information about shallow fault slip, off-fault deformation, and the coseismic strain field. We quantify the displacement discontinuities at several apertures and show the presence of inelastic and distributed off-fault deformation. Likely, the exceedance of the elastic strain threshold drove a shallow slip depletion on the primary fault trace and off-fault deformation along secondary structures. This study demonstrates that a variety of on- and off-fault deformation behavior is well recorded with high-resolution differential topography.

Acknowledgments

C. Scott was supported by NSF Postdoctoral Fellowship 1625221 and by the School of Earth and Space Exploration at Arizona State University. E. Nissen and L. Lajoie acknowledge support through the Southern California Earthquake Center through SCEC awards 14101 and 15189. We thank Manoochehr Shirzaei for a discussion on error calculation. Thanks to Koji Okumura for early conversations about the Kumamoto earthquake surface rupture. We additionally thank Yehuda Ben-Zion (Editor), Chris Milliner (reviewer), Michele Cooke (reviewer), and two anonymous reviewers for constructive comments that strengthened the manuscript. We thank the Asia Air Survey Co., Ltd. for providing us with access to the pre-earthquake and postearthquake point cloud lidar data sets. The lidar data sets are available at OpenTopography (http://www.opentopography.org). Our 3-D displacement results are included in a text file in the supporting information. The LIBICP software is available at http://www.cvlibs.net/software/libicp/.

References

Allmendinger, R. W., Cardozo, N., & Fisher, D. (2012). *Structural geology algorithms*. New York: Cambridge University Press.

Allmendinger, R. W., Loveless, J. P., Pritchard, M. E., & Meade, B. (2009). From decades to epochs: Spanning the gap between geodesy and structural geology of active mountain belts. *Journal of Structural Geology*, *31*(11), 1409–1422. https://doi.org/10.1016/j.jsg.2009.08.008

Barth, N. C., Toy, V. G., Langridge, R. M., & Norris, R. J. (2012). Scale dependence of oblique plate-boundary partitioning: New insights from LiDAR, central Alpine fault, New Zealand. *Lithosphere*, *4*(5), 435–448. https://doi.org/10.1130/L201.1

Ben-Zion, Y., Peng, Z., Okaya, D., Seeber, L., Armbruster, J. G., Ozer, N., et al. (2003). A shallow fault-zone structure illuminated by trapped waves in the Karadere-Duzce branch of the North Anatolian Fault, western Turkey. *Geophysical Journal International*, *152*(3), 699–717. https://doi.org/10.1046/j.1365-246X.2003.01870.x

Besl, P. J., & McKay, N. D. (1992). A method for registration of 3-D shapes. *IEEE Transactions on Pattern Analysis and Machine Intelligence*, *14*(2), 239–256. https://doi.org/10.1109/34.121791

Brooks, B. A., Minson, S. E., Glennie, C. L., Nevitt, J. M., Dawson, T., Rubin, R., et al. (2017). Buried shallow fault slip from the South Napa earthquake revealed by near-field geodesy. *Science Advances*, *3*(7), e1700525. https://doi.org/10.1126/sciadv.1700525

Chen, Y., & Medioni, G. (1992). Object modelling by registration of multiple range images. *Image and Vision Computing*, *10*(3), 145–155. https://doi.org/10.1016/0262-8856(92)90066-C

Chiba, T. (2018a). Pre-Kumamoto earthquake (16 April 2016) rupture lidar scan. Air Asia Survey Co., Ltd, distributed by OpenTopography. https://doi.org/10.5069/G9XP7303

Chiba, T. (2018b). Post-Kumamoto earthquake (16 April 2016) rupture lidar scan airborne lidar survey. Air Asia Survey Co., Ltd, distributed by OpenTopography. https://doi.org/10.5069/G9SX6B9T

Dolan, J. F., & Haravitch, B. D. (2014). How well do surface slip measurements track slip at depth in large strike-slip earthquakes? The importance of fault structural maturity in controlling on-fault slip versus off-fault surface deformation. *Earth and Planetary Science Letters*, *388*, 38–47. https://doi.org/10.1016/j.epsl.2013.11.043

Ekhtari, N., & Glennie, C. (2017). High-resolution mapping of near-field deformation with airborne Earth observation data, a comparison study. *IEEE Transactions on Geoscience and Remote Sensing*, *56*(3), 1598–1614. https://doi.org/10.1109/TGRS.2017.2765601.

Fialko, Y., Sandwell, D., Simons, M., & Rosen, P. (2005). Three-dimensional deformation caused by the Bam, Iran, earthquake and the origin of shallow slip deficit. *Nature*, *435*(7040), 295–299. https://doi.org/10.1038/nature03425

Fisher, N. I., Lewis, T., & Embleton, B. J. J. (1987). *Statistical analysis of spherical data*. Cambridge, UK: Cambridge University Press. https://doi.org/10.1017/CBO9780511623059

Geiger, A., Lenz, P., & Urtasun, R. (2012). Are we ready for autonomous driving? The KITTI vision benchmark suite (pp. 3354–3361). IEEE. https://doi.org/10.1109/CVPR.2012.6248074

Glennie, C. (2007). Rigorous 3D error analysis of kinematic scanning LIDAR systems. *Journal of Applied Geodesy*, *1*(3), 147–157. https://doi.org/10.1515/jag.2007.017

Goda, K., Campbell, G., Hulme, L., Ismael, B., Ke, L., Marsh, R., et al. (2016). The 2016 Kumamoto earthquakes: Cascading geological hazards and compounding risks. *Frontiers in Built Environment*, *2*. https://doi.org/10.3389/fbuil.2016.00019

Gold, R. D., Reitman, N. G., Briggs, R. W., Barnhart, W. D., Hayes, G. P., & Wilson, E. (2015). On- and off-fault deformation associated with the September 2013 M_w 7.7 Balochistan earthquake: Implications for geologic slip rate measurements. *Tectonophysics*, *660*, 65–78. https://doi.org/10.1016/j.tecto.2015.08.019

Hao, J., Ji, C., & Yao, Z. (2017). Slip history of the 2016 M_w 7.0 Kumamoto earthquake: Intraplate rupture in complex tectonic environment: Slip history of 2016 Kumamoto earthquake. *Geophysical Research Letters*, *44*, 743–750. https://doi.org/10.1002/2016GL071543

Hoshizumi, H., Ozaki, M., Miyazaki, K., Matsuura, H., Toshimitsu, S., Uto, K., et al. (2004). Geologic map of Japan 1:200,000, Kumamoto. Geological Survey of Japan, AIST.

Ikeda, M., Toda, S., Kobayashi, S., Ohno, Y., Nishizaka, N., & Ohno, I. (2009). Tectonic model and fault segmentation of the Median Tectonic Line active fault system on Shikoku, Japan. *Tectonics*, *28*, TC5006. https://doi.org/10.1029/2008TC002349

Jiang, H., Feng, G., Wang, T., & Bürgmann, R. (2017). Toward full exploitation of coherent and incoherent information in Sentinel-1 TOPS data for retrieving surface displacement: Application to the 2016 Kumamoto (Japan) earthquake. *Geophysical Research Letters*, *44*, 1758–1767. https://doi.org/10.1002/2016GL072253

Johnson, A., Flemming, R., Cruikshank, K., Martosudarmo, S., Johnson, N., Johnson, K., & Wei, W. (1997). Analecta of structures formed during the 28 June 1992 Landers-Big Bear, California earthquake sequence. *U.S.* Geological Survey Open-File Report *97–94*.

Kaneko, Y., & Fialko, Y. (2011). Shallow slip deficit due to large strike-slip earthquakes in dynamic rupture simulations with elasto-plastic off-fault response: Modelling shallow slip deficit. *Geophysical Journal International*, *186*(3), 1389–1403. https://doi.org/10.1111/j.1365-246X.2011.05117.x

Kobayashi, T. (2017). Earthquake rupture properties of the 2016 Kumamoto earthquake foreshocks (M j 6.5 and M j 6.4) revealed by conventional and multiple-aperture InSAR. *Earth, Planets and Space*, *69*(1). https://doi.org/10.1186/s40623-016-0594-y

Lewis, M. A., & Ben-Zion, Y. (2010). Diversity of fault zone damage and trapping structures in the Parkfield section of the San Andreas Fault from comprehensive analysis of near fault seismograms: Diversity of fault zone damage at Parkfield. *Geophysical Journal International*, *183*(3), 1579–1595. https://doi.org/10.1111/j.1365-246X.2010.04816.x

Li, Y.-G., Chen, P., Cochran, E. S., Vidale, J. E., & Burdette, T. (2006). Seismic evidence for rock damage and healing on the San Andreas Fault associated with the 2004 *M* 6.0 Parkfield earthquake. *Bulletin of the Seismological Society of America*, *96*(4B), S349–S363. https://doi.org/10.1785/0120050803

Li, Y.-G., & Leary, P. C. (1990). Fault zone trapped seismic waves. *Bulletin of the Seismological Society of America*, *80*(8), 1245–1271.

Lin, A., Chen, P., Satsukawa, T., Sado, K., Takahashi, N., & Hirata, S. (2017). Millennium recurrence interval of morphogenic earthquakes on the seismogenic fault zone that triggered the 2016 M_w 7.1 Kumamoto earthquake, Southwest Japan. *Bulletin of the Seismological Society of America*, *107*(6), 2687–2702. https://doi.org/10.1785/0120170149

Lin, A., & Chiba, T. (2017). Coseismic conjugate faulting structures produced by the 2016 M_w 7.1 Kumamoto earthquake, Japan. *Journal of Structural Geology*, *99*, 20–30. https://doi.org/10.1016/j.jsg.2017.05.003

Lin, A., Satsukawa, T., Wang, M., Mohammadi Asl, Z., Fueta, R., & Nakajima, F. (2016). Coseismic rupturing stopped by Aso volcano during the 2016 M_w 7.1 Kumamoto earthquake, Japan. *Science*, *354*(6314), 869–874. https://doi.org/10.1126/science.aah4629

Loveless, J. P., & Meade, B. J. (2010). Geodetic imaging of plate motions, slip rates, and partitioning of deformation in Japan. *Journal of Geophysical Research*, *115*, B02410. https://doi.org/10.1029/2008JB006248

Low, K. (2004). Linear least-squares optimization for point-to-plane ICP surface registration. *Technical Report TR04-004, Department of Computer Science,* University of North Carolina at Chapel Hill.

Marone, C. J., Scholtz, C. H., & Bilham, R. (1991). On the mechanics of earthquake afterslip. *Journal of Geophysical Research*, *96*(B5), 8441. https://doi.org/10.1029/91JB00275

Menke, W. (1984). *Geophysical data analysis: Discrete inverse theory*, *International Geophysics Series*, (Vol. 45). New York: Academic Press.

Milliner, C., Dolan, J. F., Hollingsworth, J., Leprince, S., Ayoub, F., & Sammis, C. G. (2015). Quantifying near-field and off-fault deformation patterns of the 1992 M_w 7.3 Landers earthquake: Deformation of the Landers earthquake. *Geochemistry, Geophysics, Geosystems*, *16*, 1577–1598. https://doi.org/10.1002/2014GC005693

Milliner, C., Sammis, C., Allam, A. A., Dolan, J. F., Hollingsworth, J., Leprince, S., & Ayoub, F. (2016). Resolving fine-scale heterogeneity of co-seismic slip and the relation to fault structure. *Scientific Reports*, *6*(1). https://doi.org/10.1038/srep27201

Milliner, C. W. D., Dolan, J. F., Hollingsworth, J., Leprince, S., & Ayoub, F. (2016). Comparison of coseismic near-field and off-fault surface deformation patterns of the 1992 M_w 7.3 Landers and 1999 M_w 7.1 Hector Mine earthquakes: Implications for controls on the distribution of surface strain. *Geophysical Research Letters*, *43*, 10,115–10,124. https://doi.org/10.1002/2016GL069841

Moya, L., Yamazaki, F., Liu, W., & Chiba, T. (2017). Calculation of coseismic displacement from lidar data in the 2016 Kumamoto, Japan, earthquake. *Natural Hazards and Earth System Sciences*, *17*(1), 143–156. https://doi.org/10.5194/nhess-17-143-2017

National Institute of Advanced Industrial Science and Technology (2016). Active Fault Database of Japan, October 4, 2016 version. Research Information Database DB095, National Institute of Advanced Industrial Science and Technology. Retrieved from https://gbank.gsj.jp/activefault/index_e_gmap.html

Nissen, E., Krishnan, A. K., Arrowsmith, J. R., & Saripalli, S. (2012). Three-dimensional surface displacements and rotations from differencing pre- and post-earthquake LiDAR point clouds. *Geophysical Research Letters*, *39*, L16301. https://doi.org/10.1029/2012GL052460

Nissen, E., Maruyama, T., Ramon Arrowsmith, J., Elliott, J. R., Krishnan, A. K., Oskin, M. E., & Saripalli, S. (2014). Coseismic fault zone deformation revealed with differential lidar: Examples from Japanese ~7 intraplate earthquakes. *Earth and Planetary Science Letters*, *405*, 244–256. https://doi.org/10.1016/j.epsl.2014.08.031

Okada, Y. (1985). Surface deformation due to shear and tensile faults in a half space. *Bulletin of the Seismological Society of America*, *74*, 1135–1154.

Ono, K., & Watanabe, K. (1985). Geological map of Aso volcano. In: Geological map of volcanoes. No. 4. Geological Survey of Japan.

Oskin, M. E., Arrowsmith, J. R., Corona, A. H., Elliott, A. J., Fletcher, J. M., Fielding, E. J., et al. (2012). Near-field deformation from the El Mayor-Cucapah earthquake revealed by differential LIDAR. *Science*, *335*(6069), 702–705. https://doi.org/10.1126/science.1213778

Pollard, D. D., Saltzer, S. D., & Rubin, A. M. (1993). Stress inversion methods: Are they based on faulty assumptions? *Journal of Structural Geology*, *15*(8), 1045–1054. https://doi.org/10.1016/0191-8141(93)90176-B

Riller, U., Clark, M. D., Daxberger, H., Doman, D., Lenauer, I., Plath, S., & Santimano, T. (2017). Fault-slip inversions: Their importance in terms of strain, heterogeneity, and kinematics of brittle deformation. *Journal of Structural Geology*, *101*, 80–95. https://doi.org/10.1016/j.jsg.2017.06.013

Rockwell, T. K., Lindvall, S., Dawson, T., Langridge, R., Lettis, W., & Klinger, Y. (2002). Lateral offsets on surveyed cultural features resulting from the 1999 Izmit and Duzce earthquakes, Turkey. *Bulletin of the Seismological Society of America*, *92*(1), 79–94. https://doi.org/10.1785/0120000809

Roten, D., Olsen, K. B., & Day, S. M. (2017). Off-fault deformations and shallow slip deficit from dynamic rupture simulations with fault zone plasticity. *Geophysical Research Letters*, *44*(15), 7733–7742. https://doi.org/10.1002/2017GL074323

Rusinkiewicz, S., & Levoy, M. (2001). Efficient variants of the ICP algorithm. In *Proceedings of the Third International Conference on 3-D Digital Imaging and Modeling* (pp. 145–152). Piscataway, NJ: IEEE Computer Society. https://doi.org/10.1109/IM.2001.924423

Segall, P., & Rice, J. R. (1995). Dilatancy, compaction, and slip instability of a fluid-infiltrated fault. *Journal of Geophysical Research*, *100*(B11), 22155–22171. https://doi.org/10.1029/95JB02403

Shelef, E., & Oskin, M. (2010). Deformation processes adjacent to active faults: Examples from eastern California. *Journal of Geophysical Research*, *115*, B05308. https://doi.org/10.1029/2009JB006289

Shirahama, Y., Yoshimi, M., Awata, Y., Maruyama, T., Azuma, T., Miyashita, Y., et al. (2016). Characteristics of the surface ruptures associated with the 2016 Kumamoto earthquake sequence, central Kyushu, Japan. *Earth, Planets and Space*, *68*(1), 191. https://doi.org/10.1186/s40623-016-0559-1

Simons, M., Fialko, Y., & Rivera, L. (2002). Coseismic deformation from the 1999 M_w 7.1 Hector Mine, California, earthquake as inferred from InSAR and GPS observations. *Bulletin of the Seismological Society of America*, *92*(4), 1390–1402. https://doi.org/10.1785/0120000933

Takayama, H., & Yoshida, A. (2007). Crustal deformation in Kyushu derived from GEONET data. *Journal of Geophysical Research*, *112*, B06413. https://doi.org/10.1029/2006JB004690

Teran, O. J., Fletcher, J. M., Oskin, M. E., Rockwell, T. K., Hudnut, K. W., Spelz, R. M., et al. (2015). Geologic and structural controls on rupture zone fabric: A field-based study of the 2010 M_w 7.2 El Mayor-Cucapah earthquake surface rupture. *Geosphere*, *11*(3), 899–920. https://doi.org/10.1130/GES01078.1

Toda, S., Kaneda, H., Okada, S., Ishimura, D., & Mildon, Z. K. (2016). Slip-partitioned surface ruptures for the M_w 7.0 16 April 2016 Kumamoto, Japan, earthquake. *Earth, Planets and Space*, *68*(1), 188. https://doi.org/10.1186/s40623-016-0560-8

Toth, C., Brzezinska, D., Csanyi, N., Paska, E., & Yastikli, N. (2007). LiDAR mapping sup-porting earthquake research of the San Andreas fault. *Proceedings of the ASPRS 2007 Annual Conference*. American Society for Photogrammetry and Re-Mote Sensing, 1–11.

Treiman, J. A., Kendrick, K. J., Bryant, W. A., Rockwell, T. K., & McGill, S. F. (2002). Primary surface rupture associated with the M_w 7.1 16 October 1999 Hector Mine Earthquake, San Bernardino County, California. *Bulletin of the Seismological Society of America*, *92*(4), 1171–1191. https://doi.org/10.1785/0120000923

Tsukuda, E. (1990). Active tectonics of the median tectonic line. *Bulletin of the Geological Survey of Japan*, *51*, 405–406.

Tsutsumi, H., & Okada, A. (1996). Segmentation and Holocene surface faulting on the median tectonic line, southwest Japan. *Journal of Geophysical Research*, *101*(B3), 5855–5871. https://doi.org/10.1029/95JB01913

Uchide, T., Horikawa, H., Nakai, M., Matsushita, R., Shigematsu, N., Ando, R., & Imanishi, K. (2016). The 2016 Kumamoto–Oita earthquake sequence: Aftershock seismicity gap and dynamic triggering in volcanic areas. *Earth, Planets and Space*, *68*(1), 180. https://doi.org/10.1186/s40623-016-0556-4

Vallage, A., Klinger, Y., Grandin, R., Bhat, H. S., & Pierrot-Deseilligny, M. (2015). Inelastic surface deformation during the 2013 M_w 7.7 Balochistan, Pakistan, earthquake. *Geology*, *43*(12), 1079–1082. https://doi.org/10.1130/G37290.1

Watanabe, K., Momikura, M., & Tsuruta, K. (1979). Active faults and parasitic eruption centers on the west flank of the Aso Caldera, Japan. *The Quaternary Research*, *18*(2), 89–101. https://doi.org/10.4116/jaqua.18.89

Wells, D., & Coppersmith, K. (1994). New empirical relationships among magnitude, rupture length, rupture width, rupture area, and surface displacement. *Bulletin of the Seismological Society of America*, *84*, 974–1002.

Xu, X., Tong, X., Sandwell, D. T., Milliner, C. W. D., Dolan, J. F., Hollingsworth, J., et al. (2016). Refining the shallow slip deficit. *Geophysical Journal International*, *204*(3), 1843–1862. https://doi.org/10.1093/gji/ggv563

Yagi, Y., Okuwaki, R., Enescu, B., Kasahara, A., Miyakawa, A., & Otsubo, M. (2016). Rupture process of the 2016 Kumamoto earthquake in relation to the thermal structure around Aso volcano. *Earth, Planets and Space*, *68*(1), 118. https://doi.org/10.1186/s40623-016-0492-3

Zinke, R., Hollingsworth, J., & Dolan, J. F. (2014). Surface slip and off-fault deformation patterns in the 2013 M_W 7.7 Balochistan, Pakistan earthquake: Implications for controls on the distribution of near-surface coseismic slip. *Geochemistry, Geophysics, Geosystems*, *15*, 5034–5050. https://doi.org/10.1002/2014GC005538